ACS OMEGA

http://pubs.acs.org/journal/acsodf

Article

Extended Shear Deformation of the Immiscible Cu−Nb Alloy Resulting in Nanostructuring and Oxygen Ingress with Enhancement in Mechanical Properties

Bharat Gwalani,* Qin Pang, Anqi Yu, Wenkai Fu, Lei Li, Mayur Pole, Christian Roach, Suveen N. Mathaudhu, Tanvi Ajantiwalay, Mert Efe, Shenyang Hu, Miao Song, Ayoub Soulami, Aashish Rohatgi, Yulan Li, Peter V. Sushko, and Arun Devaraj

Cite This: *ACS Omega* 2022, 7, 13721−13736

Read Online

ACCESS | Metrics & More | Article Recommendations | Supporting Information

ABSTRACT: Deformation processing of immiscible systems is observed to disrupt thermodynamic equilibrium, often resulting in nonequilibrium microstructures. The microstructural changes including nanostructuring, hierarchical distribution of phases, localized solute supersaturation, and oxygen ingress result from high-strain extended deformation, causing a significant change in mechanical properties. Because of the dynamic evolution of the material under large strain shear load, a detailed understanding of the transformation pathway has not been established. Additionally, the influence of these microstructural changes on mechanical properties is also not well characterized. Here, an immiscible Cu-4 at. % Nb alloy is subjected to a high-strain shear deformation (~200); the deformation-induced changes in the morphology, crystal structure, and composition of Cu and Nb phases as a function of total strain are characterized using transmission electron microscopy and atom probe tomography. Furthermore, a multimodal experiment-guided computational approach is used to depict the initiation of deformation by an increase in misorientation boundaries by crystal plasticity-based grain misorientation modeling (strain ~0.6). Then, co-deformation and nanolamination of Cu and Nb are envisaged by a finite element method-based computational fluid dynamic model with strain ranging from 10 to 200. Finally, the experimentally observed amorphization of the severely sheared supersaturated Cu−Nb−O phase was validated using the first principle-based simulation using density functional theory while highlighting the influence of oxygen ingress during deformation. Furthermore, the nanocrystalline microstructure shows a >2-fold increase in hardness and compressive yield strength of the alloy, elucidating the potential of deformation processing to obtain high-strength low-alloyed metals. Our approach presents a step-by-step evolution of a microstructure in an immiscible alloy undergoing severe shear deformation, which is broadly applicable to materials processing based on friction stir, extrusion, rolling, and surface shear deformation under wear and can be directly applied to understanding material behavior during these processes.

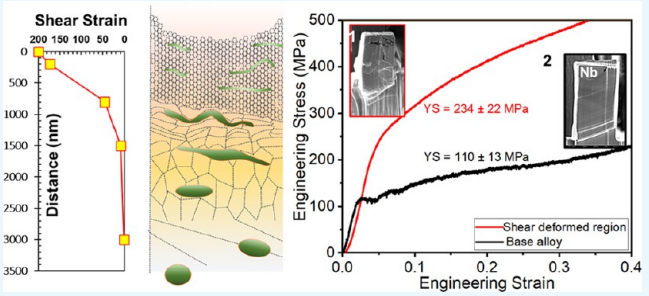

1. INTRODUCTION

Shear deformation-induced microstructural modification underpins several processing methods such as friction stir-based processing, roll bonding, drawing, and forging. The advantages of achieving highly refined and homogeneous microstructures at a relatively low cost make these deformation processing techniques extremely desirable.[1−5] However, in these processes, the dominance of mechanical mixing induced by the processing disrupts the equilibrium thermodynamic-driven atomic settlements. In addition, the inherent mechanical−thermal coupling makes it challenging to directly observe these atomic-scale diffusion events in real time. These challenges limit the knowledge of the microstructural transformation pathways during such extended shear deformation processing. Detailed work by P. Bellon and group highlights the strain-dependent modes of microstructural evolution categorized by low strain (<100), where interfacial instabilities dominate, while at high strain (>100) where the atomic mixing can be seen.[6,7] Additionally, they propose the effective temperature model to explain the observation of high solute superstation tendencies under the high-strain regime.[7,8] However, another factor that can influence the experimental observations in these processes is the interaction of the deforming material with the ambient environment, which consists of reactive gases such as oxygen. In the past,

Received: December 30, 2021
Accepted: April 8, 2022
Published: April 15, 2022

metastable supersaturated phases and amorphous structures have been reported to form in several alloys (Nb−B, Cu−Ta, Cu−Nb, and Cu−Ag) on extended deformation by mechanical alloying.[9−13] In two examples, the grain boundary excess of oxygen in nanocrystalline (NC) Al was shown to inhibit the grain boundary migration,[14] while the Zenner pinning effect of oxide nanoparticles was shown to stabilize the NC structure in the Fe−Mg ball-milled alloy.[15] Both these reports demonstrate the strong influence of oxygen on microstructural evolution and stabilization; however, the stabilization of defect-driven metastability such as amorphization due to the presence of oxygen has not been demonstrated.

The Cu−Nb alloys and composites have been widely studied due to their combination of high-mechanical strength and electrical conductivity.[11,16−18] The Cu−Nb phase diagram shows a negligibly low mutual solubility in the solid state; however, extended plastic deformation techniques such as equal channel angular extrusion[18] or high-pressure torsion (HPT)[13] have been employed to extend the region of the solid solution, resulting in a higher strength than pure Cu or Cu-based miscible alloys.[19,20] In many cases, complete solubility is not achieved; however, the fine-scale distribution of immiscible phases results in a large improvement in the mechanical properties.[17,19] The nanofibers of Nb in Cu−Nb wires increased the ultimate tensile strength of Cu from 345 to 2230 MPa.[17] In addition to strength, Kapoor et al. showed that the resistance to grain growth at elevated temperatures increases as a function of Nb concentration in Cu−Nb alloys.[21] Other techniques, such as ball milling,[22] accumulative roll bonding,[23−25] biaxial compression, and biplanar shearing,[26] are equally effective in processing Cu−Nb alloys. In the current work, we systematically reveal the influence of high-strain deformation on the microstructural evolution in an immiscible Cu−Nb system under tribological deformation in the ambient environment using a coupled experimental and computation approach. Materials undergo an extended shear strain in friction processing techniques such as friction stir processing and extrusion, where the complicated thermal and mechanical history makes the microscopic understanding of the transformation pathway very difficult. Although severe plastic deformation techniques such as HPT could introduce a large strain in the material, they are considered high-pressure techniques where total strain is less and severe plastic deformation is accomplished by the large pressure (in the order of GPa) coupled with strain. In a tribological setup, the local pressure is relatively low (in the order of MPa), while the repetitive scratching of the surface induces a high strain in the material, which results in microstructural transformation.[5,27−30] Here, the local pressure, total strain, and deformation rate can be precisely controlled relatively easily. Hence, the tribological setup was used for conducting this study. Our approach allowed us to follow the step-by-step change in the microstructure as a function of total strain, thus developing a mechanistic description of the process. In tribological tests, the plastic strain is limited, but the dislocation density due to repeated cyclic deformation can be very high, which is similar to the case of severe plastic deformation by HPT. Hence, in this work, "extended" or "severe" shear deformation are used interchangeably to define the extent of deformation.

A pin-on-disk tribometer is used to impart a high-shear strain in a Cu-4 at. % Nb (Cu−4Nb) alloy. The crystallographic and morphological changes in the dual-phase microstructure are presented as a function of shear strain. The mechanical properties accessed using indentation hardness and pillar compression testing show a massive increase in properties compared to the base alloy. A multiscale computation approach using finite element methods (FEMs), crystal plasticity-based models, and first-principle calculations complementing the experimental observations reveals the overall pathway involved in the complex microstructural changes during shear processing. The insights obtained here are crucial for developing a predictive atomic-to-mesoscale modeling approach for microstructural evolution under high-strain deformation.

2. METHODS

2.1. Materials. The binary Cu-4 at. % Nb (Cu−4Nb) alloy was cast and remelted five times for homogenization (procured from ACI alloys, California). Samples with dimensions of 20 × 10 × 3 mm cross section were cut using a slow-speed saw, mechanically ground to 2000 grit, and metallographically polished using a 0.02 μm colloidal silica solution.

2.2. Experiments. The as-cast alloy was subjected to shear deformation in dry air at room temperature using an Anton Paar pin-on-disk tribometer. A 6 mm diameter stainless steel counterface with a load of 1 N and a sliding velocity of 200 mm/s was used in the reciprocating mode for 5000 cycles, with a stroke length of 7 mm. Keyence VR-5100 white light interferometry measurements were used to determine the volume loss of the material by wear. The wear volume was then divided over the normal load and the sliding distance to obtain specific wear rates in $mm^3/N{\cdot}m$.

The microstructures of the undeformed and shear-deformed regions were characterized using scanning electron microscopy (SEM) backscattered electron (BSE) imaging, bright field transmission electron microscopy (BFTEM), high-resolution TEM (HRTEM), and atom probe tomography (APT). The sample preparation for HRTEM and APT was performed using a Thermo Fisher Scientific Quanta 200 focused ion beam (FIB)−scanning electron microscope outfitted with an Oxford Instruments energy-dispersive X-ray spectroscopy (EDS) system for compositional analysis. An Oxford Instruments electron backscatter diffraction (EBSD) detector was used for generating the inverse pole figure (IPF) maps, phase maps, and the image quality (IQ) maps for the as-cast and deformed Cu−4Nb alloy. The Cu−Nb interfaces having Kurdjumov−Sachs (KS) orientation[31] relationship with (111)Cu//(1−10)Nb and [−110]Cu//[−111]Nb were highlighted with plane and direction tolerance of 5°. The cross-sectional EBSD results presented in Figure 4 were obtained from a lamella (10 × 2 × 5 μm) lifted out using the FIB from the region of interest. After EBSD, the sample lamella was further ion milled (10 × <0.05 × 5 μm) and made electron transparent for observation under a transmission electron microscope.

For nanomechanical testing, the micropillars of dimensions 5 × 5 × 10 μm with an aspect ratio of 2:1 were fabricated using a Helios Hydra UX dual-beam plasma FIB/scanning electron microscope (PFIB). Five pillars each are milled from the base metal alloy and the shear-deformed region. The initial trenches for the pillars were made using 30 kV voltage and 60 nA to 0.20 μA currents with the xenon ion beam. The pillars were then shaped to their final dimensions at 30 kV, 1−4 nA. Micropillar compression tests were then performed using an in situ PI89 Picoindenter assembly inside the PFIB/scanning electron microscope. The compressive loading was applied using a diamond flat punch indenter in a displacement-

https://doi.org/10.1021/acsomega.1c07368
ACS Omega 2022, 7, 13721−13736

controlled fashion with a constant rate of 50 nm/s (equivalent to a strain rate of approximately 10^{-2}/s).

An FEI Titan 80−300 operated at 300 kV was used for HRTEM. CAMECA LEAP 4000X HR APT was used in the pulsed voltage mode at a 200 kHz pulse frequency with a 20% pulse fraction, a specimen temperature of 50−60 K, and a detection rate that was maintained at 0.005 atoms/pulse.

2.3. Computational Modeling. *2.3.1. Crystal Plasticity Simulation.* The crystal plasticity theory was used to study the grain misorientation in the initial stage of the co-deformation of the Cu−Nb [face-centered cubic−body-centered cubic (FCC−BCC)] bicrystal in the tribological experiments. In the crystal plasticity theory, the deformation gradient $\mathbf{F}$ is decomposed into the elastic deformation gradient ($\mathbf{F}_e$) and the plastic deformation gradient ($\mathbf{F}_p$), so that

$$\mathbf{F} = \mathbf{F}_e\mathbf{F}_p \tag{1}$$

From the elastic deformation gradient $\mathbf{F}_e$, the second Piola−Kirchhoff (PK) $\mathbf{S}$ stress is computed by

$$\mathbf{S} = \mathbb{C}\colon \mathbf{E} = \mathbb{C}\colon \left[\frac{1}{2}\left(\mathbf{F}_e^{\mathrm{T}}\mathbf{F}_e - \mathbf{I}\right)\right] \tag{2}$$

Here, $\mathbb{C}$ is the fourth-order elastic stiffness tensor of the considered material, $\mathbf{E} = \frac{1}{2}(\mathbf{F}_e^{\mathrm{T}}\mathbf{F}_e - \mathbf{I})$ is the second-order Green−Lagrange strain tensor, and the colon represents a double contraction operation. The second PK stress $\mathbf{S}$ determines the resolved shear stress τ^α in the constitutive level, which drives the plastic slip on the α slip system. The resolved shear stress τ^α is computed by Schmid's law

$$\tau^\alpha = \mathbf{S}\colon \mathbf{P}^\alpha_{\mathrm{Schmid}} \tag{3}$$

$\mathbf{P}^\alpha_{\mathrm{Schmid}}$ is the Schmid's factor defined as

$$\mathbf{P}^\alpha_{\mathrm{Schmid}} = \mathbf{s}^\alpha \otimes \mathbf{n}^\alpha \tag{4}$$

where $\mathbf{s}^\alpha$ and $\mathbf{n}^\alpha$ are the unit vectors along the shear direction and shear plane normal, respectively. In the phenomenological plastic constitutive law (or power law) used in this work, the shear strain rate of the α slip system is computed from the associated resolved shear stress by

$$\dot{\gamma}^\alpha = \dot{\gamma}_0\left|\frac{\tau^\alpha}{\xi^\alpha}\right|^{\mathrm{n}}\mathrm{sgn}(\tau^\alpha) \tag{5}$$

where the reference strain rate $\dot{\gamma}_0$ and the stress exponent n are material parameters. ξ^α is the slip resistance and evolves as follows

$$\dot{\xi}^\alpha = h_0\Sigma_{\alpha'=1}^{N_s}|\dot{\gamma}^{\alpha'}|\left|1 - \frac{\xi^{\alpha'}}{\xi_\infty^{\alpha'}}\right|^{\mathrm{a}}\mathrm{sgn}\left(1 - \frac{\xi^{\alpha'}}{\xi_\infty^{\alpha'}}\right)h^{\alpha\alpha'} \tag{6}$$

Here, N_s is the total number of slip systems. h_0, a, $\xi_\infty^{\alpha'}$, and $h^{\alpha\alpha'}$ are material parameters. h_0 and a are model-specific fitting parameters. $\xi_\infty^{\alpha'}$ is the upper bound of the slip resistance. $h^{\alpha\alpha'}$ is the component of the slip−slip interaction matrix between slip systems α and α' that describes crystal hardening, which is self-hardening for $\alpha = \alpha'$ and latent hardening for $\alpha \neq \alpha'$. The material properties of Cu and Nb are listed in Table 1.

Because of deformation heterogeneity, each grid in the representative volume element (RVE) has its orientation in the current configuration, which causes kernel average misorientation (KAM).[32] Consider two grids, k and m. $\mathbf{O}_k$ and $\mathbf{O}_m$ are their orientation matrices, respectively. The misorientation angle $\Delta\psi_{k,m}$ between grids k and m can be calculated by

$$\Delta\psi_{k,m} = \arccos\left(\frac{\mathrm{tr}(\Delta\mathbf{O}_{k,m}) - 1}{2}\right) \tag{7}$$

$$\Delta\mathbf{O}_{k,m} = \mathbf{O}_m\mathbf{O}_k^{\mathrm{T}} \tag{8}$$

The KAM angle of grid k is defined as

$$\theta_{k,\mathrm{KAM}} = \frac{1}{M_k}\sum_{m=1}^{M_k}\Delta\psi_{k,m} \tag{9}$$

where M_k is the number of the intragranular grids used for calculating $\theta_{k,\mathrm{KAM}}$, that is, the KAM angle of grid k. In this work, only the first nearest intragranular neighbors in the two-dimensional (2D) RVE were used, so $M_k \leq 4$.

2.3.2. Computational Fluid Dynamic Simulation. To further understand the material co-deformation mechanism of the Cu−Nb system under high cyclic shear strain, a mesoscale computational fluid dynamic (CFD) simulation was carried out based on the particle-in-cell FEM. This method was borrowed from a recent work on analyzing the shear-induced material mixture of metallic multilayer systems during HPT,[33] in which material phases were treated as incompressible nonlinear viscous fluids with distinct effective viscosities η_{eff} (Pa·s) following the power-law relationship.

The initial Cu−Nb morphology for the simulation was based on a cropped TEM image from an experiment with an approximate shear strain of 10. Similar to the setting in ref 33, a reference viscosity of $\eta_{\mathrm{ref}}^{\mathrm{Nb}} = 10^7$ Pa·s was assigned to the Nb material phase, whereas the Cu phase was assigned a larger reference viscosity of $\eta_{\mathrm{ref}}^{\mathrm{Cu}} = 10^8$ Pa·s (viscosity contrast = $\frac{\eta_{\mathrm{ref}}^{\mathrm{Nb}}}{\eta_{\mathrm{ref}}^{\mathrm{Cu}}} = 10$). The power-law component n or the effective viscosity exponent was set to 3. The VC^n value determines the morphing mechanism of Nb, and a value of 3 was recognized empirically by comparing it with the experiment. The physical significance of n in a solid-state immiscible system is still unknown. Simple cyclic shear boundary conditions with a strain rate of 100 s^{-1} estimated from the experiment were applied on the top and bottom surfaces, while periodic boundary conditions were considered on the left and right

Table 1. Material Properties of Cu and Nb Used in the Crystal Plasticity Simulation[a]

property	Cu	Nb
crystal structure	FCC	BCC
C_{11} (GPa)	168	250
C_{12} (GPa)	121	135
C_{44} (GPa)	75.4	30
$\dot{\gamma}_0$ (ms^{-1})	0.001	0.001
ξ_0 (MPa)	16	95/97
ξ_∞ (MPa)	148	222/413
h_0 (MPa)	180	1000
coplanar $h^{\alpha\alpha}$	1	1
non-coplanar $h^{\alpha\alpha'}$ ($\alpha \neq \alpha'$)	1.4	1.4
n	83.3	20
a	2.25	2

[a]FCC has one slip system family, and BCC has two slip system families. Each slip system family has 12 slip systems. For Nb, ξ_0 and ξ_∞ of these two slip families are listed.

https://doi.org/10.1021/acsomega.1c07368
ACS Omega 2022, 7, 13721−13736

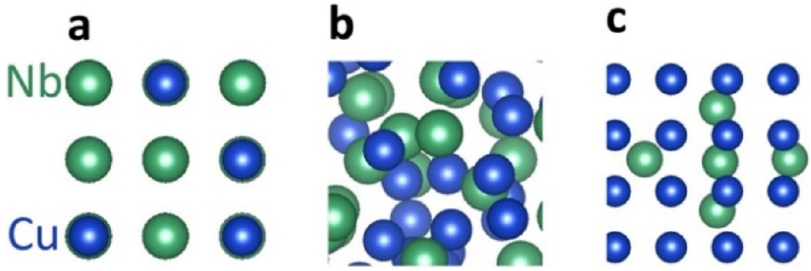

Figure 1. Illustration of the studied models for the Cu−Nb system. (a) Crystalline model (random substitutional sites). (b) Amorphous model (randomly distributed Cu and Nb atoms). (c) Segregated crystalline model.

surfaces of the simulation domain. For each shearing cycle, the simulation domain undergoes 0.6 shear strain. It took 316 cycles to achieve the target shear strain of 200.

2.3.3. Density Functional Theory. We used three models to represent the Cu−Nb systems (Figure 1), including a crystalline model with substitutional Nb in FCC Cu and substitutional Cu in BCC Nb, an amorphous model with randomly distributed Cu and Nb atoms, and a segregated crystalline model with a distorted crystalline lattice in the crystalline host. These models are referred to as crystalline, amorphous, and segregated crystalline models, respectively, hereafter.

The density functional theory (DFT)[34,35] calculations were performed using the Vienna Ab initio Simulation Package[36−39] with the Perdew−Burke−Ernzerhof exchange−correlation functional[40,41] and the projector-augmented wave potential.[42] The plane-wave basis set with an energy cutoff of 369.3 and 500 eV was used for Cu−Nb systems without and with interstitial O, respectively. The Γ point alone was used for all the calculations. The self-consistent field energy convergence criterion was set at 10^{-5} eV. The convergence criteria for energy minimization were set as 0.05 eV/Å for the amorphous systems due to their complexity, but 10^{-4} eV for the other systems. All the configurations are fully relaxed with respect to cell shape and size and internal atomic positions. The charge distribution was analyzed using the Bader charge.[43−46] The computed lattice parameters for Cu and Nb were 3.642 and 3.323 Å, respectively, in good agreement with the experimental values.[47,48]

The energy with respect to FCC Cu, BCC Nb, and gas-phase O_2 used to quantify the stability of the Cu−Nb or Cu−Nb−O systems is calculated using eq 10

$$\Delta E = (E_{sys} - E_{Cu} \times n_{Cu} - E_{Nb} \times n_{Nb} - E_{O_2}/2 \times n_O) / (n_{Cu} + n_{Nb} + n_O) \quad (10)$$

where E_{sys} is the total energy of the Cu−Nb or Cu−Nb−O system. E_{Cu} and E_{Nb} are the energies of the bulk Cu and Nb, respectively, per atom. The n_{Cu} and n_{Nb} are the numbers of Cu and Nb atoms in the system, respectively. The total number of Cu and Nb atoms ($n_{Cu} + n_{Nb}$) is 500, except for the segregated crystalline model, for which the total number of atoms varies due to the different densities of atoms in the FCC Cu and BCC Nb. The Nb concentration [Nb] is calculated as $n_{Nb}/(n_{Cu} + n_{Nb})$. E_{O2} is the energy of O_2 in the gas phase, and n_O (n_O = 1) is the total number of O in the Cu−Nb−O system.

For the crystalline model, a fraction of the FCC Cu atoms were replaced with Nb and, conversely, a fraction of the BCC Nb atoms were replaced with Cu. In both cases, the Nb concentration varied from 0 to 100%. The locations of the Nb_{Cu} and Cu_{Nb} sites were chosen at random; m configurations were considered for each Nb concentration (m = 3 in most cases). Then, their energies were weighted with Boltzmann factors

$$w_i = e^{-\frac{\delta E_i}{k_B T}} \quad (11)$$

where δE_i is the energy of configuration i with respect to the lowest energy for each Nb concentration, k_B is the Boltzmann constant, and T is the temperature. In the absence of information on the local temperature during processing, we set the temperature used to calculate w_i to 1000 K.

The weighted average total energy was calculated as

$$E_{sys} = \underset{m}{(E_i \times w_i)/w_i} \quad (12)$$

Similarly, the weighted average fractions of FCC or BCC phases for each Nb concentration were calculated using eq 13

$$\text{fraction} = \underset{m}{(f_i \times w_i)/w_i} \quad (13)$$

where f_i is the fraction of the BCC or FCC phase in the configuration i.

3. RESULTS AND DISCUSSION

3.1. Starting Microstructure: Cu−4Nb Alloy. The starting material in our work is a bulk as-cast Cu−4Nb alloy (methods section) where the Cu forms the large-grained matrix phase while the Nb phase (particles) is dispersed in the form of spherical and near-spherical microprecipitates (the bright contrast phase in the BSE images in Figure 2a). The Cu grain size is >500 μm, and the particle size for Nb is ∼1.5 ± 0.2 μm. The EBSD maps (IPF map, phase map, and IQ map in Figures 2b1 and 3) show that the Nb particles in Cu are randomly orientated. We do not observe a strict orientation relationship between all of the Nb−Cu interfaces in this as-cast condition; however, ∼65% of the boundaries observed a KS orientation[31] relationship with (111)Cu//(1−10)Nb and [−110]Cu//[−111]Nb (Figure 2b3).

The BFTEM (Figure 2c1) confirms that the Nb particles are spherical, and the corresponding EDS maps (Figure 2c1) together with the selected area electron diffraction (SAED) patterns (Figure 2c2,c3) consistently index the Nb-rich phase/particle as BCC and the Cu-rich phase as FCC. The compositional analysis of the two phases (Nb-rich and Cu-rich) was carried out using APT (Figure 2d), depicting extremely low solubility of Nb in the Cu matrix (<0.01 at. %) (Figure 2d1) and of Cu in Nb particles (<0.01 at. %) (Figure 2d2).

3.2. Tribological Deformation Using a Pin-on-Disk Tribometer. Tribological experiments were performed in dry

https://doi.org/10.1021/acsomega.1c07368
ACS Omega 2022, 7, 13721−13736

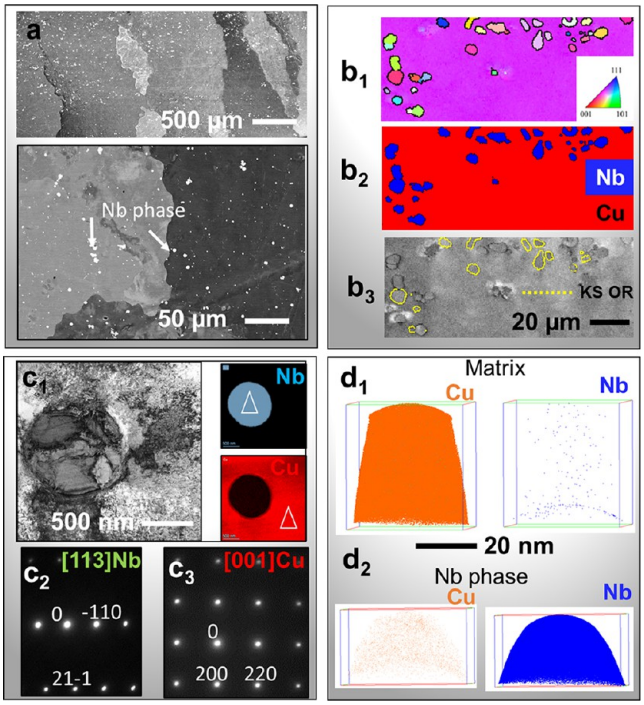

Figure 2. Cu-4 at. Nb starting microstructure. (a) SEM image with the Nb phase (bright contrast particles) dispersed in the Cu matrix. (b) EBSD results show stress-relieved grains of Cu with the IPF in b1, the phase map in b2, and the IQ map overlaid with KS OR [(111)Cu//(1−10)Nb and [−110]Cu//[−111]Nb)] boundaries in b3. (c) TEM results ambiguously show the FCC Cu matrix and spherical BCC Nb particles. (d) Composition of each phase is measured using APT, where d1 shows the reconstruction of the representative needle prepared from the Cu matrix and d2 is from the Nb phase. The Cu phase has <0.05 at. % Nb while the Nb phase shows ∼0.5 at. % Cu dissolved in it.

air at room temperature using an Anton Paar pin-on-disk tribometer (parameters are described in Methods).

After characterizing, the starting alloy condition, the polished top surface of the specimen was shear deformed by moving the tribometer pin reciprocally forward and backward on the surface of the sample, creating a wear track. Figure 3 describes the observations from the surface-wear test on the Cu−4Nb sample, where Figure 3a has a 2D wear depth and wear width plot after 5000 sliding reciprocal cycles on the surface. The inset shows the optical inferometry image of the wear track, which is used to estimate the wear rate in the alloy. The steady-state coefficient of friction (COF) was calculated to be 0.58 ± 0.05, while the wear rate was $6.2 \pm 0.3 \times 10^{-4}$ $mm^3/N{\cdot}m$ (Figure 3b). The COF versus sliding cycles shows an initial rise in the COF values till 2000 cycles, and then it stabilizes. The very early variation in the COF, which is the initial run-in period (<300 cycles), corresponds to the removal of the nascent oxide layer on the alloy and the initial grooving on the surface to attain a perfect mating between the surface and the counterface. The depth versus sliding cycles in Figure 3c suggests that the rapid depth increase (negative direction) occurred at ∼100 cycles, which was then stabilized at 300 cycles, while the rapid increase in the COF starts at ∼500 cycles when the depth remains constant. This indicates material on the top of the surface undergoes high-strain deformation without being removed after 500 cycles. Thus, it can also be indicative of the material hardening resulting from the deformation; hence, the rapid increase in the COF is observed.[49−51] The strong influence of microstructural changes on the COF is further highlighted in Figure 3d, where the COF is plotted from 0−100, 300−400, 1000−1100, and 4000−4100 sliding cycles. A three times increase in the COF was noticed as the material underwent strain hardening and resists the removal process.

3.3. Microstructural Characterization of the Sheared Region Below the Tribometer Wear Track (Strain <1).

This study is interested in the sheared region below the wear track as a function of total deformation. Hence, FIB foils for TEM characterization were lifted out along the wear track after 1/2, 10 (low-strain deformation), and 5000 cycles (high-strain deformation). After a single scratch (1/2 cycle), we observed the shearing of a prior twin boundary to estimate the shear deformation experienced by the Cu matrix phase (Figure S1). The apparent shear strain of 0.32 was calculated using $\gamma = \cot\alpha\text{-}\cot\beta$, where γ is the shear strain and β and α are the initial and final angles, respectively, that the twin boundary makes with the surface. Note that the shearing of the twin boundary takes place by twin migration, leaving the ledges on the parent twin boundary consistent with some prior observations.[52]

We now examine the 10-cycle condition. The EBSD results consisting of the IQ and IPF after 10 cycles of deformation are shown in Figure 4a,b respectively. The sample was prepared along the sliding direction by the FIB lift-out technique and put through EBSD, followed by final ion milling/cleaning before TEM examination. The Nb phase in the FIB lamella was indexed with low confidence and hence is masked using black color while the Cu phase was indexed with high confidence. However, the EDS maps (Figure 4c−e) conclusively show that the unindexed and elongated regions in the EBSD map are Nb-rich.

The deformation in the large-grained Cu matrix proceeds with grain fragmentation and rotation. The region 1 μm below the wear track consisted of highly refined grains (∼200 nm), and one such grain is highlighted using a white arrow in Figure 4b. The Nb particles become elongated due to shear deformation, and a high density of dislocation loops is observed in the Nb phase [scanning TEM (STEM) image in Figure 4f,g]. The formation of these dislocation loops near the Cu−Nb interfaces has been associated with the collapsing of lattice planes after the aggregation of profuse vacancies induced during severe shear deformation.[53] We also note that the dislocation-free twin interacting with the phase boundary creates a rugged pattern on the interface (Figure 4h). The nucleation of twin structures on the phase boundary and the growth of them in Cu will facilitate further refinement of Cu grains.[54,55] The formation of these dislocation-free twins is proposed to be induced by severe stress concentration on the rugged interface.[56] Based on our earlier estimation of apparent shear strain in the Cu matrix after 1/2 cycle (∼0.3), the total apparent strain after 10 cycles can be estimated to be ∼6. The average particle size of the Nb phase in the as-cast microstructure was ∼1.5 μm, and the deformed diameter of the Nb ellipsoid was measured to be ∼0.5 μm. The shear strain induced in the Nb phase can be estimated to be 3 (Figure S2). Hence, we note that the strain accumulated in the Nb particle is about half of what is estimated for the Cu phase if the strain accumulation was assumed to be linearly increasing. However, the work hardening of the Cu phase can reduce the strain accumulation in Cu as a function of the number of cycles. Additionally, a limited dislocation-assisted strain transfer from

https://doi.org/10.1021/acsomega.1c07368
ACS Omega 2022, 7, 13721−13736

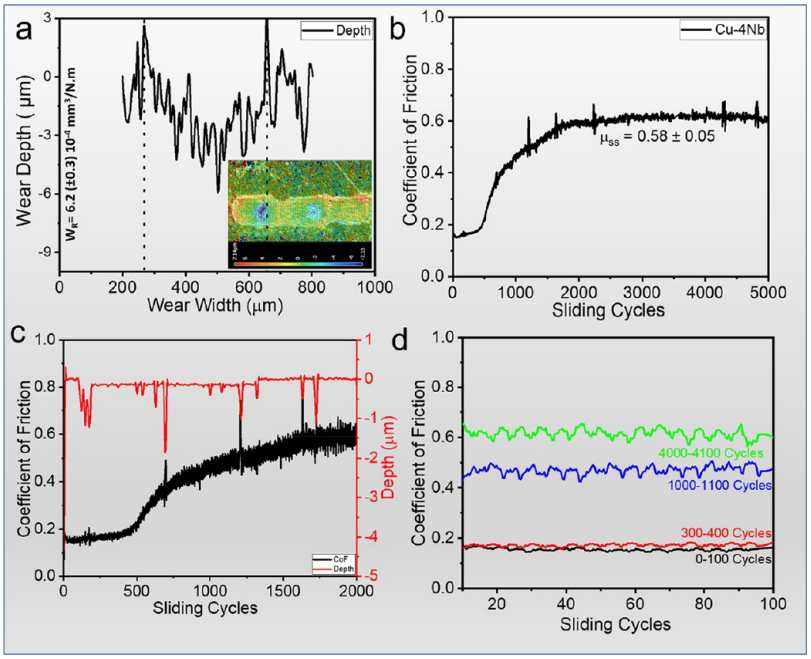

Figure 3. Tribological testing on the Cu−4Nb alloy. (a) Wear depth versus wear width after 5000 cycles [(inset) optical image of the wear track from the top of the track]. (b) COF versus the number of cycles shows an initial increase in the COF, which is stabilized after ∼2000 cycles. (c) Initial regime of the COF versus the number of cycles and wear depth versus the number of cycles are plotted together to compare the starting point of increase in the COF with material loss. (d) COF in different ranges of the number of cycles is plotted to show an increase in the COF with material deformation.

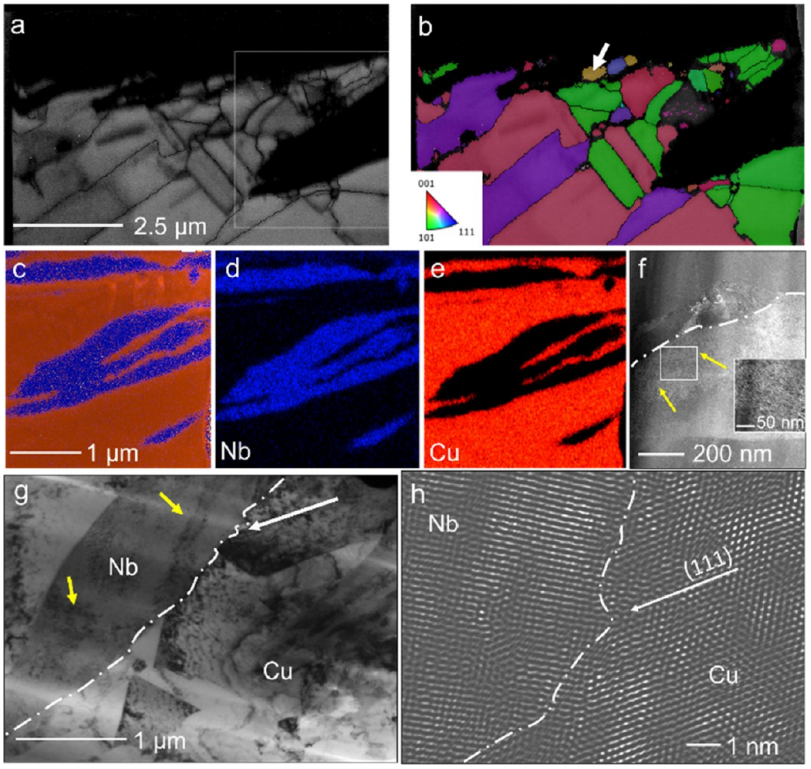

Figure 4. Subsurface microstructural characterization after 10 cycles of tribological testing along the sliding direction: (a) IQ map showing the deformed Cu grains, (b) IPF map, (c) composition map showing Cu (orange) and Nb (blue) from the section highlighted in (a) using a white box, (d,e) individual Nb and Cu maps, respectively. (f) STEM image showing the interface between Cu and Nb phases after shearing, and (g) BFTEM and (h) HRTEM images showing the rugged Cu−Nb interface.

the Cu matrix to the Nb particles through the partically coherent or noncoherent interfaces can result in a lower shear deformation of the Nb phase. An accurate estimation of the strain versus sliding cycle function would involve observations of material removal, redeposition, work hardening, and microstructural changes at each step. This needs an in situ

https://doi.org/10.1021/acsomega.1c07368
ACS Omega 2022, 7, 13721−13736

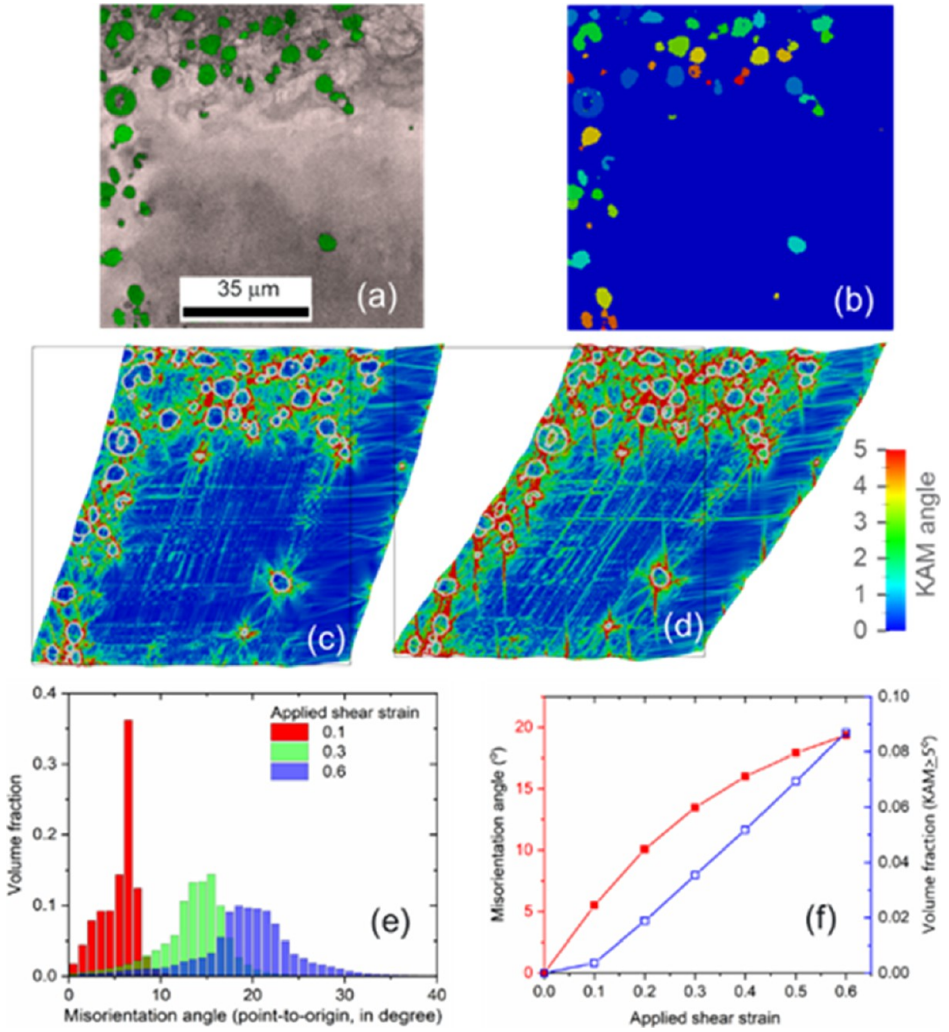

Figure 5. (a) SEM image from experimental measurement where Nb precipitates are in green. (b) RVE is used for the crystal plasticity simulation where the matrix is a single Cu grain (in blue) and Nb precipitates with different orientations (in colors). (c) RVE with 30% shear deformation (1/2 cycle). (d) RVE with 60% shear deformation (1 cycle). The color in (c,d) represents the KAM angle indicated by the given color bar. The red region depicts its KAM angle ≥5°. (e) Histograms of misorientation angles vary with the applied shear strain. The misorientation angle refers only to the material points in the Cu grain relative to its original orientation. (f) Average misorientation angle to its origin in Cu varies with the applied shear strain (in red), and the volume fraction of KAM ≥ 5° varies with the applied shear strain (in blue).

tool to observe material deformation while testing and is not the focus of the current work. Hence, the linear extrapolation of strain based on the measurement performed after initial deformation cycles is conducted as an approximation to guide computational simulations for comparison with the experimental results in the current work.

To understand the initiation of plastic deformation at very low strain (<1 strain), we used a crystal plasticity-based computation simulation method.

3.4. Simulation of Early-Stage Deformation under Cyclic Shear Loading. The crystal plasticity theory has been successfully applied to study different phenomena in Cu−Nb bicrystals with layered structures deformed under the rolling process. The investigated phenomena included the heterophase interface stability,[57] the effects of the interface-affected zone,[58] and the effects of layer thickness on the deformation mechanism[59] and strength[60] of the layered Cu−Nb bicrystal. Figure 5 depicts the initial RVE and deformed RVEs with misorientation angle distributions. The initial RVE (Figure 5b) was constructed from the SEM image (Figure 5a). Figure 5c,d illustrate the deformed RVE and the colors on it show the KAM angle distribution.

The histograms of the misorientation angles at the three deformation stages are summarized in Figure 5e. The misorientation angles and volume fractions of KAM ≥ 5° varying with the applied shear strain are given in Figure 5f. It is seen that the misorientation angles increase with increased deformation. Larger KAM angles occurred around the Nb precipitates. This is because the presence of Nb precipitates resulted in deformation inhomogeneity that caused local large plastic deformation. Because large misorientation will induce grain fragmentation, the simulation results imply that grain refinement may happen around the precipitates first. The experimental result in Figure 4h depicts the nucleation of the twin boundary from the rugged Nb−Cu interface after 10 cycles (total strain ∼3). However, our simulation results show that before the high-stress concentration needed for the nucleation of the twin, the deformation proceeds with the formation of low-angle boundaries. Our simulation results also indicate a very limited plastic deformation in the Nb particles

https://doi.org/10.1021/acsomega.1c07368
ACS Omega 2022, 7, 13721−13736

in the early stage of deformation due to interfacial strengthening, which is consistent with experimental observations of the lower shearing response of the Nb phase after 10 cycles discussed earlier.

3.5. Microstructural Characterization after High-Shear Deformation Below the Tribometer Wear Track (Strain >1). Now we study the microstructural evolution after a high-shear strain deformation induced after 5000 cycles of tribological testing (Figure 6). The wear track from the top

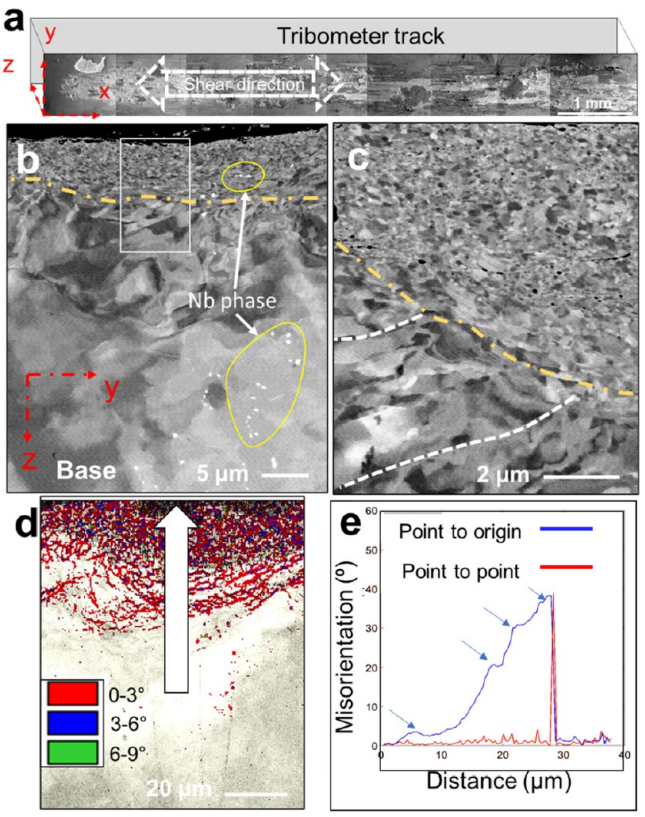

Figure 6. SEM examination of the subsurface shear deformed microstructure after the tribological experiment (across the sliding direction). (a) SEM image of the wear track. Based on the assigned x, y, and z directions, the tribometer pin moved in the x-direction, the width of the track is the y-direction, and the depth of the track (subsurface) is the z-direction. (b) Cross-sectional SEM image with the highly refined grain structure below the track extends to ∼7 μm. The strain contrast due to deformation can be seen extending to ∼30 μm. The Nb particles are highlighted by the yellow arrow in the figure. (c) Higher magnification SEM image of the region marked by a white square in (b). NC grains are visible here, and a sharp change in grain size is evident beyond ∼7 μm, marked by a yellow dotted line. (d) EBSD result showing the misorientation boundaries, with the misorientation angle ranging from 0 to 5. A high density of misorientation boundaries with 1−3° misorientation is observed below the tribometer track. (e) One-dimensional (1D) misorientation profile is drawn from the base to the wear track, showing a gradual strain accumulation and increase in misorientation from the base.

view can be seen in Figure 6a, where the different directions (x, y, z) are highlighted on the bottom left corner of Figure 6a. The z-direction depicts the direction extending below the track, while x and y represent the length and breadth in the top view, respectively. A cross-sectional BSE image showing the z−y plane displays the extent of the deformed microstructure extending ∼30 μm below the surface, where the top 5 μm has a highly refined grain structure (delineated with a yellow dotted line) in Figure 6b,c.

Some bright contrast Nb particles are encircled by yellow boundaries and highlighted by white arrows in Figure 6b. The particles are observed to be elongated in the NC Cu matrix region near the top, while they are close to spherical morphology in the less deformed lower region of the sample. The IQ map overlayed with the misorientation boundaries in Figure 6d shows a high density of 1−3° boundaries formed in the high-shear region. A misorientation profile from the base to the sheared region displays the gradual change in the lattice orientation as the shear strain increases (Figure 6e). The gradual change in the point to origin misorientation as a function of distance from the base depicts the formation of low-angle boundaries and deformation bands in the matrix, while the plateaus in the plot (highlighted by arrows in Figure 6e) correspond to the large-angle boundaries.[61,62] This means that this region is still at an early stage of dynamic recrystallization and the crystal lattice is severely deformed. The point-to-point misorientation profile (red line in Figure 6e) shows spikes in the region close to the surface, suggesting the formation of NC grains with large-angle boundaries; that is, dynamic recrystallization has already finished. This NC region is detailed further in our TEM examination in Figure 8.

3.6. Comparison of Mechanical Properties of the Base Alloy and the Shear-Deformed Region. The composition map clearly illustrates the microstructural changes in the z−x plane (along the sliding direction) below the wear track (Figure 7). The Cu and Nb maps plotted using SEM−EDS highlight the formation of Nb-rich nanofibers or whiskers near the top (<5 μm below the track), while further below (>5 μm), the particles are still elongated but much thicker (Figure 7a). The thickness of the Nb particle changes from nano to micronscale going from the top region to the base, depicting the change in shear strain experienced by the material. To measure the change in the mechanical properties as a function of distance from the surface, we used microindentation (Vicker's hardness) and nanopillar compression on the base and deformation processed alloy. The hardness in the base varied between 75 and 93 Hv based on the density of heterogeneously precipitated Nb particles. The regions with a higher density of Nb particles measured a higher hardness, likely due to interfacial strengthening. However, the hardness increases steeply in the highly sheared region with the redistribution of Cu−Nb phases. The maximum hardness measured was ∼270 Hv close to the surface. Figure 7b shows the 2-D map of the hardness distribution below the wear track. To compare the stress−strain behavior of the processed and base alloy under compression, we conducted nanomechanical testing using rectangular pillars as shown in Figure 7c. Apart from the sheared Cu and Nb phases, we also noted a heavy ingress of O in the alloy that probably occurred during testing (oxygen map in Figure 7c). More details on oxygen distribution in the deformed microstructure are obtained using APT and will be presented later. The comparison of stress−strain behavior (Figure 7d) clearly shows an increase in yield stress from ∼110 MPa in the base alloy to ∼234 MPa in the sheared region, consistent with the hardness measurements.

3.7. Calculation of Shear Strain as a Function of Distance from the Surface and the CFD Model for Depicting Co-Deformation of Cu−Nb under High-Strain Cyclic Shear Deformation. The elongation and redistrib-

https://doi.org/10.1021/acsomega.1c07368
ACS Omega 2022, 7, 13721−13736

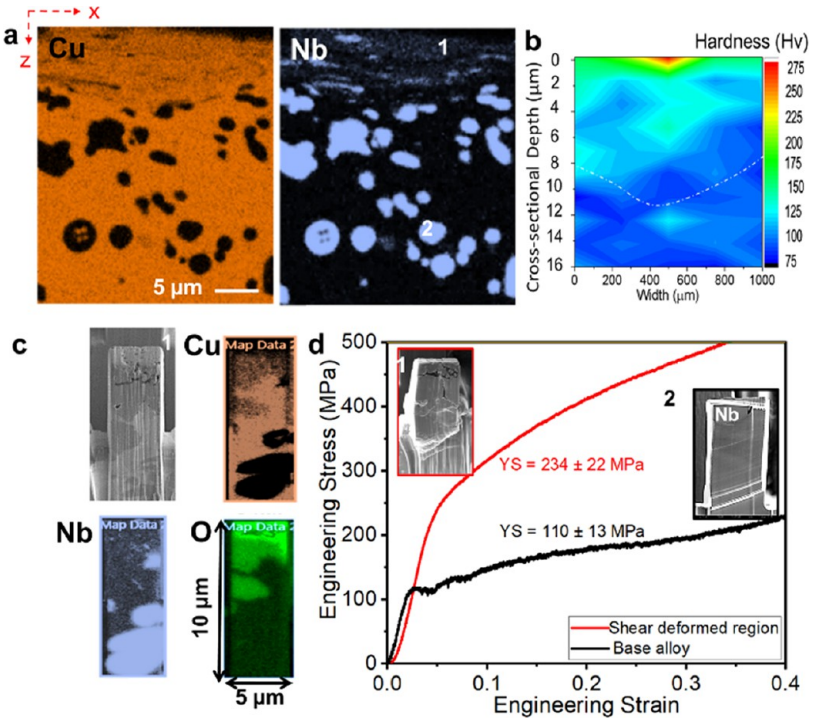

Figure 7. Cross-sectional microstructure below the wear track and the comparison of mechanical properties in the sheared region with the base alloy (along the shear direction): (a) SEM−EDS results with the Cu and Nb phase distributions below the wear track. (b)Vicker's hardness distribution (2D map) as a function of depth from the surface below the wear track. The *y*-axis shows the depth in microns (on the left) and hardness values in Hv (on the right), while the *x*-axis shows the width of the region that was characterized. The white dotted line delineates the shear region on top of the base. (c) Micropillars (5 * 5 * 10 μm) were loaded in compression and the SEM image and EDS maps with Cu, Nb, and O are shown. (d) Engineering stress−strain curves are shown from two representative regions (1 and 2), which are marked on the Nb map (b).

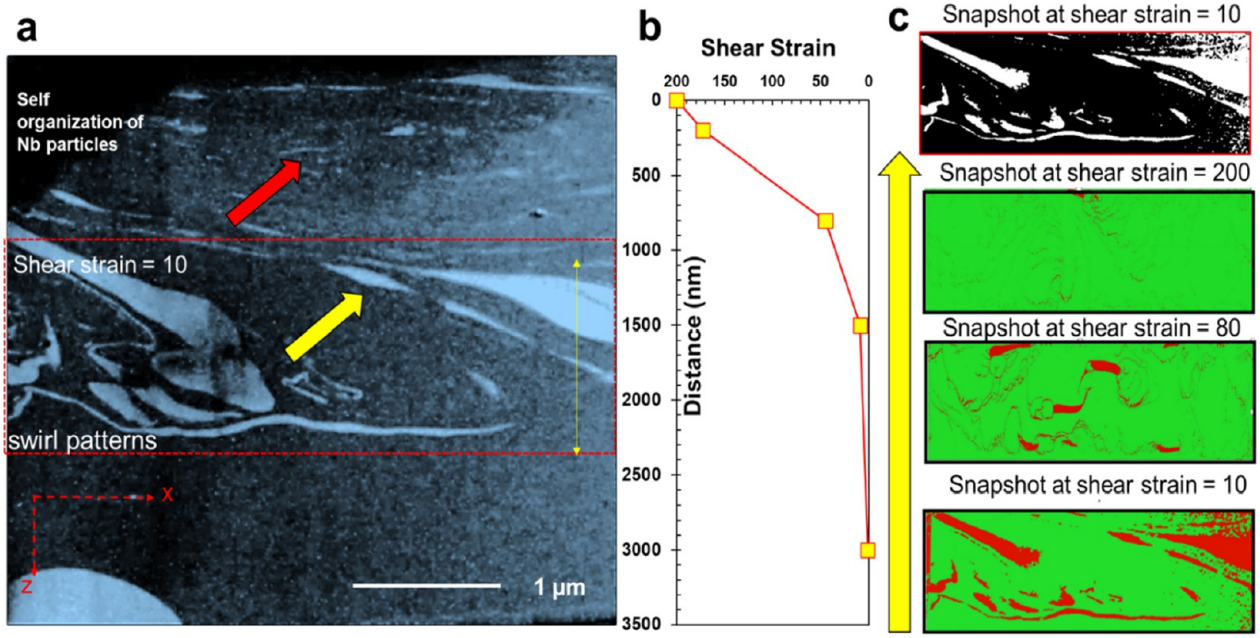

Figure 8. Simulated pathway for the formation of nanofibers of the Nb phase. (a) Nb composition map is performed using TEM−EDS, showing a high-magnification image where the highly refined nanofibers of Nb can be seen. (b) Shear strain below the wear track is estimated using the shape change of the Nb particle below the wear track. The plot shows the distribution of shear strain as a function of depth. The maximum shear strain experienced near the surface is ∼200. (c) Top image is the TEM image showing the region of interest used for the FEM-based CFD model. The evolution of the Cu and Nb phases as the strain is increased from 10 to 200 under the cyclic loading below the tribometer pin.

ution seen in the SEM results in Figure 7 are more clearly seen in the TEM results in Figure 8a. Self-organization and nanolamination of Cu and Nb phases can be seen, as pointed out by the red arrow in Figure 8a (∼1 μm below the wear track). The average thickness of the Nb fibers in this region varies from 5 to 50 nm, while below this region the average

https://doi.org/10.1021/acsomega.1c07368
ACS Omega 2022, 7, 13721−13736

thickness increases to ~100 nm, as pointed out by the yellow arrow. Dautzenberg and Zaat[63] devised a method to estimate the plastic strain for a spherical grain under simple shear: $\varepsilon \sim D/(\sqrt{3}c)$ $(D \gg c)$, where D is the diameter of the initial grain/particle and c is the thickness of the sheared grain/particle. The maximum strain near the top surface (100 nm below the surface), where the thickness of the Nb phase is ~5 nm, is estimated to be ~173, while it reduces to 30 at 500 nm below the surface and to 6 at 1500 nm below the wear track. The change in shear strain is plotted as the distance from the wear track (where zero is considered close to the top surface and the maximum shear strain is extrapolated to be ~200 here) in Figure 8b, which seems to approximately follow an exponential decay as a function of depth.

It is also seen that the deformation proceeds with material removal (Figure 3), and hence the material may be worn away before achieving the theoretical maximum strain by extrapolating from 1 or 10 cycles. Cai and Bellon et al.[30] estimated the strain as a function of depth on a eutectic Ag−Cu alloy after the tribometer test, indicating a plastic strain of ~7.4 in the subsurface. The microstructure and solute solubility have been discussed as a function of total strain in the past. For instance, Hughes et al. noted that under small to medium strain (ε = 0.06−0.8), long microbands and dense dislocation walls are formed, while at large strain (ε > 1), lamella boundaries parallel to the deformation direction are formed, in which are cells or equiaxed subgrains.[64] Beach et al. studied Nb in the solid solution as a function of strain using HPT.[65]

We notice a striking difference in the microstructural refinement in the top 1 μm region compared to the next 1 μm region below it. From our estimation, the shear strain in the region 1−2 μm from the top is ~10 (highlighted by the red box in Figure 8a). To observe the microstructural transformation from a shear strain of 10−200, an FEM-based CFD model was employed in which two material phases were treated as non-Newtonian fluids with different viscosities. The simulation results are summarized in Figure 8c.

As shown in Figure 8a, when the shear strain increases, the existing Nb swirl patterns will elongate, fold, and vortex under the cyclic shear loading, whereas the smaller Nb particles are gradually dispersed into the Cu matrix and mixed with the Cu material phase. The elongated Nb swirl patterns become thinner due to the dispersion of their boundary Nb particles into the surrounding Cu phase. Finally, at the high-shear strain of 200, most of the Nb phase is dispersed into the Cu matrix, with only a few thin Nb swirls existing. This trend is in good agreement with the high-shear strain region shown in the top 1 μm region in Figure 8a, in which a more complete microstructural refinement is achieved with only smaller Nb swirls remaining in the domain. To envisage the morphological changes in the Nb phase as a function of shear strain, a short video is provided in the Supporting Information.

3.8. Structure and Morphology of Cu and Nb after Maximum Shear Strain. Further details on the microstructural evolution of Cu−4Nb as a function of the depth under the wear track are obtained by using detailed examination in TEM (Figure 9). Figure 9a is a BFTEM image that shows that the Cu matrix microstructure evolves from a NC(grain size 10−20 nm) grain to a relatively coarser ultrafine grain (UFG, grain size ~165 nm at 3000 nm below the wear track). The SAED patterns embedded in Figure 9a are consistent with the grain size change. The region near the surface (<0.5 μm below the wear track) has an average Cu

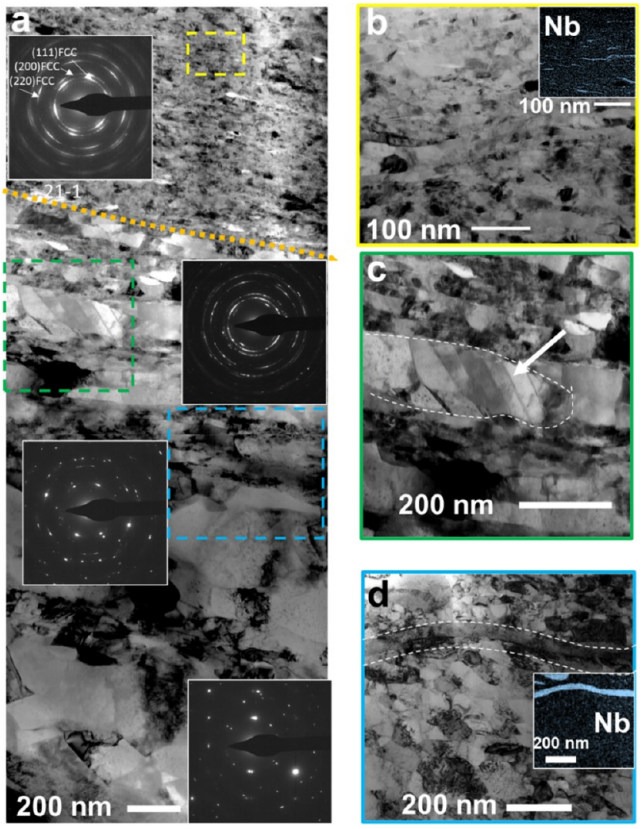

Figure 9. TEM characterization of the shear deformation layer below the wear track. (a) BFTEM image with the grain size distribution from 0 nm (wear track) to 3000 nm below the wear track. The SAEDs from the different regions are given in the inset. (b) High-magnification BFTEM image of the region highlighted by a yellow box in (a). Nanostrings of the Nb phase are seen in the Nb EDS map of this region, given as the inset. (c) High-magnification BFTEM image of the region highlighted by a green box in (a). Deformation twins in the Cu phase can be seen in this region. (d) High-magnification BFTEM image of the region highlighted by a blue box in (a). This region shows larger Cu grains and thicker Nb nanofibers in comparison to those seen in (a,b).

grain size of ~16 nm (Figure 9b). The SAED from this region depicts a ring pattern, indicating a highly randomized NC structure. An EDS map of Nb embedded in Figure 9b shows nanofibers of the Nb phase in this region. Below the NC region, there is an obvious transition to the UFG region, in which twinning (Figure 9c) and elongated Nb particles (Figure 9d) are observed. The twin boundaries in the deformed Cu phase are noted in two conditions in our analysis (Figure 4 after 10 cycles, and in Figure 9 after 5000 cycles of sliding wear deformation). On both occasions, the twin boundaries are a little below the surface of the sample. We expect the heat dissipation in our process to be very fast, thus limiting the formation of annealing twins in the region closest to the surface. However, the frictional heat that is dissipated into the subsurface region could assist in the formation of dislocation-free twins in the refined Cu grain structure. At ~1.5 μm below the wear track, the Cu grain size tends to become stable at ~165 nm. It is worth mentioning that although this region shows a coarser microstructure than the area near the surface, it is still very refined compared with the initial Cu grain size (>500 μm) in Figure 2a. The refinement and redistribution of the Nb phase along the Cu grain boundaries during the

https://doi.org/10.1021/acsomega.1c07368
ACS Omega 2022, 7, 13721−13736

deformation-induced nanocrystallization stabilizes the refined grain structure of Cu.[5,54,66] Both the refined Cu grains and the observation of the elongated Nb-rich phase indicate that tribological shearing is still affecting the microstructure ~3 μm below the wear track. However, the larger grain size and thicker Nb-rich phase indicate that the total strain in this region is lower than in the region closest to the wear track (<500 nm).

To further understand the structure and composition of the two phases in the sheared region, we conducted a detailed examination employing HRTEM and APT analysis. Figure 10

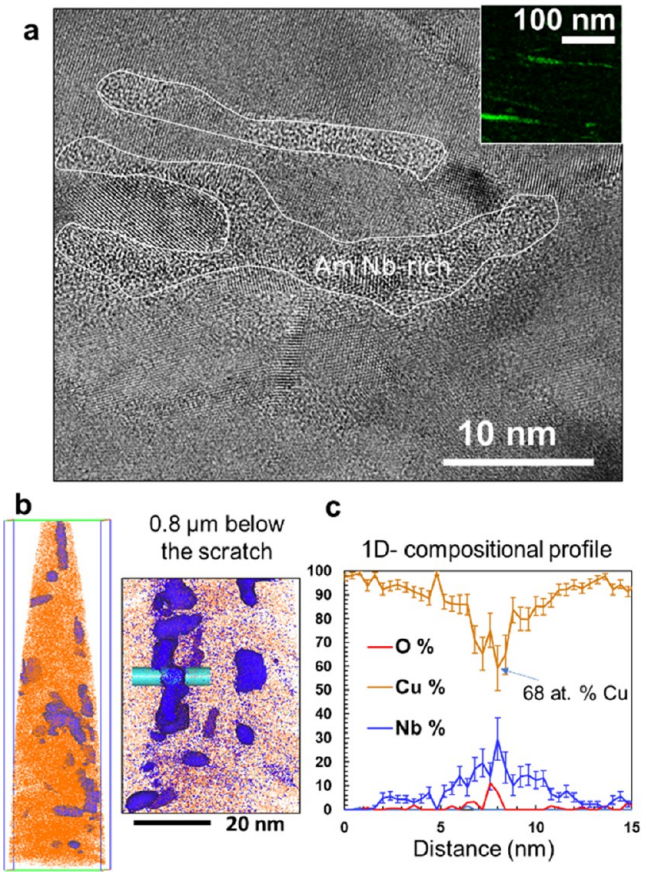

Figure 10. Characterization of highly deformed Nb-rich nanofibers. (a) HRTEM image of the Nb-rich nanofiber at 200 nm below the wear track shows an amorphous structure. (b) Composition and three-dimensional distribution of these nanofibers were observed using APT. (c) 1D compositional profile across one such fiber depicting the compositional change across the phase.

has a high-resolution phase contract TEM image showing that amidst the NC Cu grains, the Nb fibers lose their crystallinity, resulting in localized amorphization of these Nb-enriched pockets (Figure 10a). On further examination of the composition of these amorphous fibers using APT (Figure 10b), we notice that even though the Nb concentration in these pockets is higher than that in the matrix, the fibers are highly enriched in Cu (>68 at. %). Apart from Cu and Nb, we also see oxygen enrichment in these Nb whiskers. As the tribological testing was performed in the ambient environment, the ingress of oxygen into the topmost shear region is practically unavoidable considering the high affinity of Nb for oxygen. A summary of the composition of the Nb and Cu phases versus distance, obtained by making APT needles at different locations below the wear track, is given in Table 2 and plotted in Figure 11. The amorphization of the Nb phase and

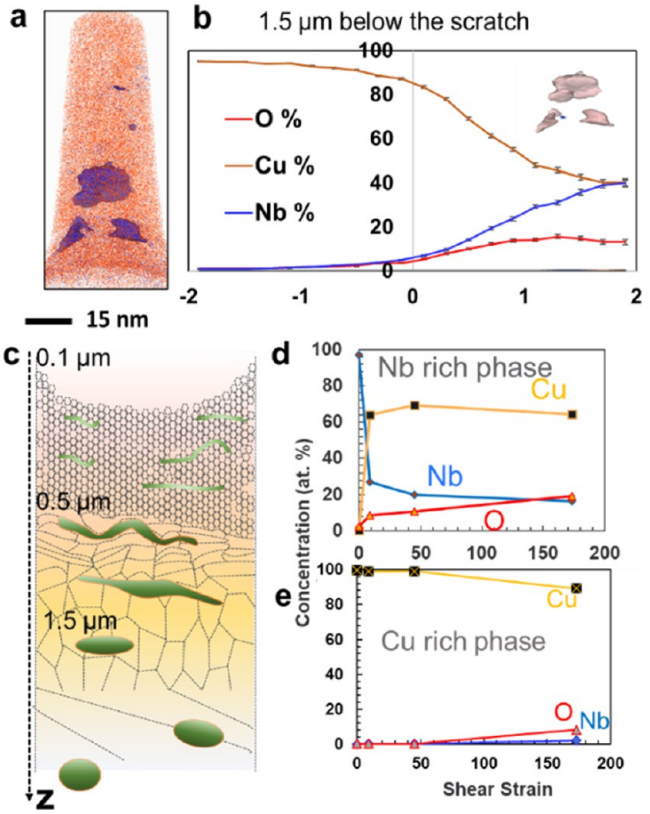

Figure 11. Compositional change as a function of strain below the wear track. (a) APT reconstruction shows the Cu- and Nb-rich phases at 1.5 μm below the wear track. (b) Proximity histogram plotting across the Cu−Nb interface (Nb 10 at. %). (c−e) Composition of Cu- and Nb-rich phases as a function of strain.

the Cu−Nb phase boundary after high-strain shear or high-shear stress loading has been reported in previous work and has been explained based on the forced mixing mechanism.[67,68] Ashkenazy et al. used large-scale molecular dynamics simulations to show that an amorphous phase is stable beyond a strain of 400 in dilute Cu−Nb, Cu−Ta, and Cu−V alloys.[6]

Table 2. Composition of Nb- and Cu-Rich Phases as the Function of Total Estimated Strain Below the Wear Track

	Nb phase (at. %)						Cu phase (at. %)					
total strain	Nb	error	Cu	error	O	error	Nb	error	Cu	error	O	error
173	16.35	0.14	64.35	0.53	19.3	0.25	1.97	0.23	89.22	2.43	8.1	0.58
45	20.16	0.15	69.2	0.58	10.64	0.04	0.24	0.02	99.05	0.47	0.1	0.01
9	27.21	0.32	64.11	0.59	8.68	0.19	0.09	0	98.9	0.17	0.09	0.01
0	96.96	0.2	0.49	0.05	2.55	0.3	0.04	0.05	99.7	0.1	0.1	0.01

https://doi.org/10.1021/acsomega.1c07368
ACS Omega 2022, 7, 13721−13736

Amorphization was also seen at some of the Cu−Nb interfaces after heavy wire drawing (true strain: η = 10.5), which was interpreted in terms of the thermodynamic destabilization of a Cu−Nb crystalline phase between 35 and 80 at. % Cu.[11] Similarly, the amorphization in the Cu−Ta system has been observed with a concentration ranging from Cu20Ta to Cu70Ta.[10] These observations indicate that the amorphous phase in the immiscible system forms within a certain chemical composition under high-shear strain. In our study, the composition of the maximum strain region was accessed using APT, evincing ∼2 at. % Nb in the NC Cu, where the total strain is estimated to be ∼173. The cyclic mode of shear deformation in the current study could accelerate the forced solubility and induce higher solute and lower strain compared to HPT; however, the presence of oxygen and amorphization is critically assessed using first-principle calculations in Section 3.8.

The composition of the Nb-rich phase is observed to change as a function of distance from the top surface and thus as a function of total strain. Figure 11 summarizes the compositional changes in the Cu-rich matrix and the Nb-rich particle as a function of strain. The APT reconstruction in Figure 11a is from the region that is 1.5 μm below the wear track. A proximity histogram across the Cu−Nb interface plotted in Figure 11b shows, even in this region (strain ∼9), a high Cu (>40 at. %) and O (>10 at. %) partition toward the Nb-rich phase (average composition as a function of strain is given in Table 2).

Figure 11c schematizes the morphological observations of Cu and Nb phases below the wear track, and Figure 11d,e show the composition of each phase as a function of strain. It is noted that the supersaturation of Cu in the Nb phase reaches >60 at. % at ∼10 strain and remains at that level even when the strain is increased to ∼200. The O ingress is notable in the Nb-rich phase. The O in starting Nb was ∼2.5 at. %, while in the highly shear amorphous Nb-rich phase it is ∼19.3 at. %.

3.9. Amorphization of Nb-Rich Phase: First-Principles-Based Calculation. To better understand the formation of the amorphous phase from the crystalline phase, the stability of crystalline and amorphous structures was investigated using three types of Cu−Nb models (see Figure 1). For the crystalline model, we investigated the Nb-poor and Nb-rich separately by incorporating Nb impurities into the Cu FCC host and Cu impurities into the Nb BCC host, respectively. The positive energy change ΔE for all the models (Figure 12a) suggests that all the studied configurations are thermodynamically unstable with respect to the bulk FCC Cu and BCC Nb. The stability of the crystalline Cu−Nb systems decreases with increasing impurity concentration, while the dominant phase is retained up to [Nb] ∼ 25% in the Nb-poor system and down to [Nb] ∼ 50% in the Nb-rich system. The weighted fractions of the FCC and BCC phases at each Nb concentration (Figure 12b) show the competition between the FCC and BCC phases in the interval of Nb concentrations of 25−60%, which suggests the possible formation of amorphous Cu−Nb regions.

Our attempts to model amorphous Cu−Nb by randomly arranging the Cu and Nb atoms in the simulation supercell and minimizing the energy concerning the atomic positions and simulation cell parameters resulted in configurations that are noticeably less stable than the crystalline structures (Figure 12a). Furthermore, their stability decreases with the increasing Nb concentration; this effect of the disorder on the stability is

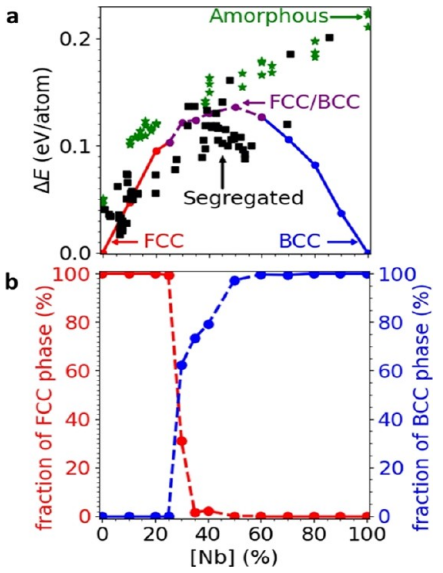

Figure 12. (a) Energy cost of forming intermixed Cu−Nb systems for three types of models. Red and blue highlight the region where the dominant phases are FCC and BCC, respectively. Purple shows the transition region with a mixture of FCC and BCC phases. (b) Fraction of FCC and BCC phases in the fully relaxed crystalline model is shown in panel (a). The dashed lines correspond to the transition region [see panel (a)], in which the presence of both FCC and BCC phases is observed.

consistent with the higher cohesive energy of Nb than that of Cu: 7.57 and 3.49 eV/atom, respectively.

Finally, we considered the model of segregated Cu and Nb regions by representing them as crystalline spherical inclusions incorporated into a crystalline host and relaxing these combined structures. Because Nb is the minor component of the experimentally considered systems, we focused on the range of Nb concentrations up to ∼60%. In this case, we found a large fraction of the considered configurations were more stable than the configurations of the crystalline model, as shown in Figure 12a. In particular, we found that segregation of Nb inclusions and Nb dissolution into the Cu FCC phase compete at low Nb concentrations (<15%), while segregation clearly dominates at [Nb] of 20∼60%.

The energy profile and fraction of the local crystalline phases (Figure 12) suggest that the Cu−Nb system is more stable as an FCC crystalline structure at a smaller Nb concentration but more stable as a BCC crystalline structure at a larger Nb concentration. Full relaxation of the configurations in the crystalline model leads to the appearance of the co-existing region of FCC and BCC phases; this region is especially prominent in the range of 30−40% Nb. An alternative model of co-existing FCC and BCC phases considered here, albeit for segregated Cu and Nb, respectively, shows that in the range of ∼20−55% Nb, the formation of segregated Cu and Nb regions is thermodynamically preferred (Figure 12). In the limit of small Nb inclusions in Cu and vice versa, the interface-induced deformations are sufficient to make these regions partially amorphous (see Figure S3), which is consistent with the formation of the amorphous phase as shown in Figure 10.

The structural parameters of all the relaxed configurations are analyzed using the excess volume, bond length distribution, and angle distribution (see Figure S4). The dependence of excess volume on the Nb concentration (Figure S4a) shows a

https://doi.org/10.1021/acsomega.1c07368
ACS Omega 2022, 7, 13721−13736

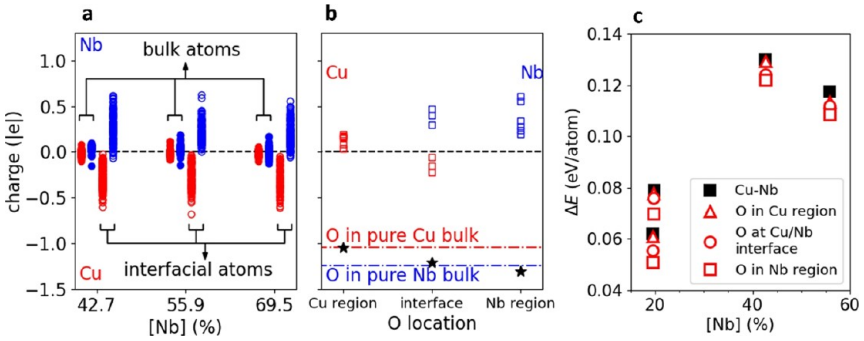

Figure 13. Charge distribution in selected crystalline phase-segregated Cu−Nb (a) and Cu−Nb−O (b) systems. (a) Cu (red) and Nb (blue) atomic charges in the oxygen-free Cu−Nb show a strong disproportionation of the electron charge at the Cu/Nb interface, while the inner atoms remain neutral in both Cu and Nb regions. (b) Interstitial O species in Cu−Nb−O (Nb concentration of 42.7%) further oxidize Nb and create a distribution of positively and negatively charged Cu species depending on their proximity to the interface. (c) Calculated enthalpy of the Cu−Nb systems decreases with the addition of oxygen; the stabilizing effect of interstitial O is most prominent if it is located in the Nb-rich regions.

trend similar to that of ΔE (Figure 12a), as expected for immiscible systems: as the fraction of Nb in Cu increases, so does the Cu−Nb interfacial area, resulting in a larger contribution of Cu−Nb repulsion into the total energy. We note the excess volume calculated for the segregated crystalline model is generally larger than that for the crystalline model, which is attributed to the existence of explicit Cu/Nb interfaces that facilitate local structural reorganization, resulting in the larger excess volume and lower interfacial energy cost. The widths of the distribution of the bond lengths and angles with the nearest neighbors for all the considered models reach their maxima at [Nb] ∼ 30−50% (Figure S4). Among the three models, the amorphous and segregated crystalline models are less ordered than the crystalline model, which is attributed to the random atomic arrangements in the amorphous model and the interfacial distortions and partial amorphization in the segregated Cu−Nb model.

The charge distribution (Figure 13a) in selected configurations of the segregated crystalline models shows that the bulk atoms (i.e., atoms located away from the Cu/Nb interface), both Cu and Nb, are nearly neutral, suggesting that the Cu−Nb charge redistribution is confined to their interface only. Interfacial charge transfers between Cu and Nb results in positively charged Nb and negatively charged Cu atoms, which is consistent with their relative electronegativities of 1.9 and 1.6 for Cu and Nb, respectively.

The calculated charges of Cu, Nb, and interstitial O in Cu−Nb−O are shown in Figure 13b. Specific O locations within the Cu region were selected so that all the atoms within 3 Å of these O atoms, that is, within one or more coordination shells, are Cu atoms only. The same approach was used for O in Nb. For the interface, we used sites that correspond to relatively large excess volumes. The charge population analysis suggests that O atoms preferentially oxidize neighboring Nb rather than Cu atoms. This suggests that O atoms preferentially oxidize neighboring Nb rather than Cu atoms, thus creating electrostatic interaction between positive Nb and negative O species which stabilizes interstitial oxygens (O_i). Indeed, the calculated stability of O_i at selected locations in Cu−Nb (see Supporting Information Table S1) suggests that O_i is most stable in the Nb bulk region, which is consistent with the experimentally observed higher O concentration in the Nb-rich region (Figure 11).

The effect of interstitial O on the overall stability of selected segregated crystalline Cu−Nb systems is shown in Figure 13c. The lower values of ΔE energies indicate the stabilization brought about by the incorporation of a single O_i. The calculated effect matches the dependence of the O_i stability on its local environment: it is the weakest in the Cu-rich regions and the strongest in the Nb-rich regions.

4. CONCLUSIONS AND SUMMARY

We studied the extended shear deformation of an immiscible Cu−Nb alloy. A cyclic shear deformation using pin-on-disk tribometer results in a strain accumulation in the material, which increases as a function of sliding cycles. Our work demonstrates the step-by-step evolution of the microstructure, starting from an early stage of deformation to a highly strained condition. Our observations are summarized in the following points:

1) A combination of experimental observations and crystal plasticity-based grain misorientation modeling showed the initiation of plastic deformation by misorientation boundaries concentrated around the Cu−Nb interface.
2) Continuous shearing results in the co-deformation of phases, which is depicted by using a CFD finite element model, presenting the pathway for microstructural changes resulting in the formation of Nb-rich nanofibers. Extreme deformation caused both localized supersaturation and nanocrystallization. The deformation proceeds with the elongation of the Nb phase accommodated by high dislocation density while elongation and pronounced nanocrystallization in the Cu phase. The concentration of Nb in the Cu grain decreases from a maximum of 2 at. % near the surface to <0.05 at. % in the base alloy. The Nb-rich phase forms nanofibers and exists in an amorphous structure near the surface, enduring the highest-shear strain deformation.
3) The shear-deformed microstructure showed a >2-fold increase in the compressive yield strength when compared to the base alloy. A comparison of the hardness values of different Cu-binary alloys (lean and concentrated) is given in Figure S5. The hardness of pure Cu increases from 40 to 75 Hv on the addition of 4 at. % Nb and to 95 Hv in Cu-50 at. % Nb (all the alloys in large-grained as-cast condition). Although the hardness of the Cu−4Nb alloy increased to 270 Hv after deformation processing. Hence, it clearly shows that extended solid-state shear processing can be a highly

https://doi.org/10.1021/acsomega.1c07368
ACS Omega 2022, 7, 13721−13736

efficient method to develop low-solute high-strength alloys.

4) DFT simulations suggest that segregation of crystalline-like Nb and Cu regions is thermodynamically preferred if the local concentration of Nb exceeds ∼20%. However, in the case of small Nb inclusions (∼100−250 atoms), interfacial Cu−Nb interactions alone induce deformations that may be manifested as the amorphization of the Nb inclusions. Simulations also show the Cu−Nb systems are stabilized by O atoms, especially when the O atom is placed in the Nb bulk region, which is consistent with the stronger bonding of O with Nb than with Cu.

Our current approach using a tribometer presents a high-throughput method to study alloys under severe plastic deformation as a function of total strain. Our experimental results, coupled with computational simulations, reveal that deformation-induced microstructural evolution, and metastable solute saturated phases with distinctive defect structures can result from high-shear strain processes. The influence of oxygen on high-strain deformation processing in creating metastable structures and modifying the transformation pathway is distinctively highlighted by this work.

■ ASSOCIATED CONTENT

Supporting Information

The Supporting Information is available free of charge at https://pubs.acs.org/doi/10.1021/acsomega.1c07368.

CFD shear deformation Cu−Nb (MOV)

Calculation of shear strain after 1 scratch in pure Cu by twin boundary migration under strain, shear strain after 10 cycles in the Nb particle examples of Cu−Nb structural models used in ab initio computational modeling, dependence of excess volume (ΔV) on Nb concentration [Nb], comparison of Vicker's hardness versus metal/alloy condition, and stability of interstitial O (O_i) in selected Cu−Nb configurations in the segregated crystalline model, pure Cu (FCC), and Nb (BCC) (PDF)

■ AUTHOR INFORMATION

Corresponding Author

Bharat Gwalani − *Physical and Computational Sciences Directorate, Pacific Northwest National Laboratory, Richland, Washington 99352, United States;* orcid.org/0000-0002-3021-6676; Email: bharat.gwalani@pnnl.gov

Authors

Qin Pang − *Physical and Computational Sciences Directorate, Pacific Northwest National Laboratory, Richland, Washington 99352, United States*

Anqi Yu − *Physical and Computational Sciences Directorate, Pacific Northwest National Laboratory, Richland, Washington 99352, United States*

Wenkai Fu − *Physical and Computational Sciences Directorate, Pacific Northwest National Laboratory, Richland, Washington 99352, United States*

Lei Li − *Energy and Environment Directorate, Pacific Northwest National Laboratory, Richland, Washington 99352, United States*

Mayur Pole − *Physical and Computational Sciences Directorate, Pacific Northwest National Laboratory, Richland, Washington 99352, United States*

Christian Roach − *Energy and Environment Directorate, Pacific Northwest National Laboratory, Richland, Washington 99352, United States*

Suveen N. Mathaudhu − *Energy and Environment Directorate, Pacific Northwest National Laboratory, Richland, Washington 99352, United States; Material Science and Engineering Program, University of California, Riverside, California 92521, United States; Colorado School of Mines, Golden, Colorado 8040, United States*

Tanvi Ajantiwalay − *Physical and Computational Sciences Directorate, Pacific Northwest National Laboratory, Richland, Washington 99352, United States*

Mert Efe − *Energy and Environment Directorate, Pacific Northwest National Laboratory, Richland, Washington 99352, United States*

Shenyang Hu − *Physical and Computational Sciences Directorate, Pacific Northwest National Laboratory, Richland, Washington 99352, United States*

Miao Song − *Physical and Computational Sciences Directorate, Pacific Northwest National Laboratory, Richland, Washington 99352, United States*

Ayoub Soulami − *Energy and Environment Directorate, Pacific Northwest National Laboratory, Richland, Washington 99352, United States*

Aashish Rohatgi − *Energy and Environment Directorate, Pacific Northwest National Laboratory, Richland, Washington 99352, United States*

Yulan Li − *Physical and Computational Sciences Directorate, Pacific Northwest National Laboratory, Richland, Washington 99352, United States;* orcid.org/0000-0002-2431-5408

Peter V. Sushko − *Physical and Computational Sciences Directorate, Pacific Northwest National Laboratory, Richland, Washington 99352, United States;* orcid.org/0000-0001-7338-4146

Arun Devaraj − *Physical and Computational Sciences Directorate, Pacific Northwest National Laboratory, Richland, Washington 99352, United States;* orcid.org/0000-0003-1314-6212

Complete contact information is available at: https://pubs.acs.org/10.1021/acsomega.1c07368

Notes

The authors declare no competing financial interest.

■ ACKNOWLEDGMENTS

This work was supported by the Laboratory Directed Research and Development program at the Pacific Northwest National Laboratory (PNNL) as part of the Solid Phase Processing Science initiative. A portion of this research was performed using facilities at the Environmental Molecular Sciences Laboratory, a national scientific user facility sponsored by the U.S. Department of Energy's (DOE's) Office of Biological and Environmental Research and located at PNNL. The ab initio calculations were performed using the PNNL Institutional Computing service. PNNL is a multiprogram national laboratory operated by Battelle for the DOE under Contract DEAC05-76RL01830. S.P. and S.V. acknowledge funding from

the NSF MRI #1726897 and DOE DE-NE0008739 for this work.

REFERENCES

(1) Miranda, R. M.; Gandra, J. P.; Vilaca, P.; Quintino, L.; Santos, T. G. *Surface modification by solid state processing*; Woodhead Publishing, 2013.
(2) Rathee, S.; Maheshwari, S.; Siddiquee, A. N.; Srivastava, M. A review of recent progress in solid state fabrication of composites and functionally graded systems via friction stir processing. *Crit. Rev. Solid State Mater. Sci.* **2018**, *43*, 334−366.
(3) Sahoo, S. K.; Toth, L. S.; Molinari, A.; Latypov, M. I.; Bouaziz, O. Plastic energy-based analytical approach to predict the mechanical response of two-phase materials with application to dual-phase steels. *Eur. J. Mech. Solid.* **2022**, *91*, 104414.
(4) Toth, L. S.; Vu, V. Q.; Dhinwal, S. S.; Zhao, Y.; Massion, R.; Chen, C.; Davis, C. F.; Lowe, T. C. The mechanics of High Pressure Compressive Shearing with application to ARMCO® steel. *Mater. Charact.* **2019**, *154*, 127−137.
(5) Toth, L. S.; Chen, C.; Pougis, A.; Arzaghi, M.; Fundenberger, J.-J.; Massion, R.; Suwas, S. High pressure tube twisting for producing ultra fine grained materials: a review. *Mater. Trans.* **2019**, *60*, 1177−1191.
(6) Ashkenazy, Y.; Pant, N.; Zhou, J.; Bellon, P.; Averback, R. S. Phase evolution of highly immiscible alloys under shear deformation: Kinetic pathways, steady states, and the lever-rule. *Acta Mater.* **2017**, *139*, 205−214.
(7) Bellon, P.; Averback, R. S.; Ren, F.; Pant, N.; Ashkenazy, Y. A Review: Microstructural and Phase Evolution in Alloys during Extended Plastic Deformation. *JOM* **2021**, *73*, 2212−2224.
(8) Pant, N.; Verma, N.; Ashkenazy, Y.; Bellon, P.; Averback, R. S. Phase evolution in two-phase alloys during severe plastic deformation. *Acta Mater.* **2021**, *210*, 116826.
(9) Linker, G. Strain induced amorphization of niobium by boron implantation. *Solid State Commun.* **1986**, *57*, 773−776.
(10) Veltl, G.; Scholz, B.; Kunze, H.-D. Amorphization of Cu Ta alloys by mechanical alloying. *Mater. Sci. Eng. A* **1991**, *134*, 1410−1413.
(11) Raabe, D.; Ohsaki, S.; Hono, K. Mechanical alloying and amorphization in Cu−Nb−Ag in situ composite wires studied by transmission electron microscopy and atom probe tomography. *Acta Mater.* **2009**, *57*, 5254−5263.
(12) Zhou, J.; Averback, R. S.; Bellon, P. Stability and amorphization of Cu−Nb interfaces during severe plastic deformation: Molecular dynamics simulations of simple shear. *Acta Mater.* **2014**, *73*, 116−127.
(13) Permyakova, I. E.; Glezer, A. M.; Karpov, M. I.; Vnukov, V. I.; Shtansky, D. V.; Gorshenkov, M. V.; Schetinin, I. V. Structure Amorphization and Mechanical Properties of Nanolaminates of the Copper−Niobium System During High-Pressure Torsion. *Russ. Phys. J.* **2018**, *61*, 428−438.
(14) He, M.-R.; Samudrala, S. K.; Kim, G.; Felfer, P. J.; Breen, A. J.; Cairney, J. M.; Gianola, D. S. Linking stress-driven microstructural evolution in nanocrystalline aluminium with grain boundary doping of oxygen. *Nat. Commun.* **2016**, *7*, 1−9.
(15) Amram, D.; Schuh, C. A. Interplay between thermodynamic and kinetic stabilization mechanisms in nanocrystalline Fe-Mg alloys. *Acta Mater.* **2018**, *144*, 447−458.
(16) Greer, A. L.; Karpe, N.; Bøttiger, J. Diffusional aspects of the solid state amorphization reaction. *J. Alloys Compd.* **1993**, *194*, 199−211.
(17) Bevk, J.; Harbison, J. P.; Bell, J. L. Anomalous increase in strength of insitu formed Cu-Nb multifilamentary composites. *J. Appl. Phys.* **1978**, *49*, 6031−6038.
(18) Summers, T. S. E.; Segal, V. M.; Hartwig, K. T.; Goforth, R. E.; Walsh, R. P.; Pernambuco-Wise, P. ECAE-processed Cu-Nb and Cu-Ag nanocomposite wires for pulse magnet applications. In *Advances in Cryogenic Engineering Materials*; Springer, 1996; pp 499−505.
(19) Yang, W.; Beyerlein, I. J.; Jin, Q.; Ge, H.; Xiong, T.; Yang, L.; Pang, J.; Zhou, Y.; Shao, X.; Zhang, B.; Zheng, S.; Ma, X. Strength and ductility of bulk Cu/Nb nanolaminates exposed to extremely high temperatures. *Scr. Mater.* **2019**, *166*, 73−77.
(20) Mara, N. A.; Bhattacharyya, D.; Dickerson, P.; Hoagland, R. G.; Misra, A. Deformability of ultrahigh strength 5 nm Cu/ Nb nanolayered composites. *Appl. Phys. Lett.* **2008**, *92*, 231901.
(21) Kapoor, M.; Kaub, T.; Darling, K. A.; Boyce, B. L.; Thompson, G. B. An atom probe study on Nb solute partitioning and nanocrystalline grain stabilization in mechanically alloyed Cu-Nb. *Acta Mater.* **2017**, *126*, 564−575.
(22) Nasu, T.; Nagaoka, K.; Takahashi, S.-y.; Suganuma, E.; Sekiuchi, T.; Fukunaga, T.; Suzuki, K. SEM Observation on Solid State Amorphization of Ni−Nb Alloy by Ball Milling. *Mater. Trans., JIM* **1989**, *30*, 620−623.
(23) Moering, J.; Ma, X.; Chen, G.; Miao, P.; Li, G.; Qian, G.; Mathaudhu, S.; Zhu, Y. The role of shear strain on texture and microstructural gradients in low carbon steel processed by Surface Mechanical Attrition Treatment. *Scr. Mater.* **2015**, *108*, 100−103.
(24) Botcharova, E.; Heilmaier, M.; Freudenberger, J.; Drew, G.; Kudashow, D.; Martin, U.; Schultz, L. Supersaturated solid solution of niobium in copper by mechanical alloying. *J. Alloys Compd.* **2003**, *351*, 119−125.
(25) Nizolek, T. J.; Begley, M. R.; McCabe, R. J.; Avallone, J. T.; Mara, N. A.; Beyerlein, I. J.; Pollock, T. M. Strain fields induced by kink band propagation in Cu-Nb nanolaminate composites. *Acta Mater.* **2017**, *133*, 303−315.
(26) Vo, N. Q.; Averback, R. S.; Ashkenazy, Y.; Bellon, P.; Wang, J. Forced chemical mixing at Cu-Nb interfaces under severe plastic deformation. *J. Mater. Res.* **2012**, *27*, 1621.
(27) Laube, S.; Kauffmann, A.; Ruebeling, F.; Freudenberger, J.; Heilmaier, M.; Greiner, C. Solid solution strengthening and deformation behavior of single-phase Cu-base alloys under tribological load. *Acta Mater.* **2020**, *185*, 300−308.
(28) Haug, C.; Ruebeling, F.; Kashiwar, A.; Gumbsch, P.; Kübel, C.; Greiner, C. Early deformation mechanisms in the shear affected region underneath a copper sliding contact. *Nat. Commun.* **2020**, *11*, 839.
(29) Cai, W.; Bellon, P.; Beaudoin, A. J. Probing the subsurface lattice rotation dynamics in bronze after sliding wear. *Scr. Mater.* **2019**, *172*, 6−11.
(30) Cai, W.; Bellon, P. Subsurface microstructure evolution and deformation mechanism of Ag−Cu eutectic alloy after dry sliding wear. *Wear* **2013**, *303*, 602−610.
(31) Wang, J.; Kang, K.; Zhang, R. F.; Zheng, S. J.; Beyerlein, I. J.; Mara, N. A. Structure and property of interfaces in ARB Cu/Nb laminated composites. *Jom* **2012**, *64*, 1208−1217.
(32) Gwalani, B.; Fu, W.; Olszta, M.; Silverstein, J.; Yadav, D. R.; Manimunda, P.; Guzman, A.; Xie, K.; Rohatgi, A.; Mathaudhu, S.; Powell, C. A.; Sushko, P. V.; Li, Y.; Devaraj, A. Lattice misorientation evolution and grain refinement in Al-Si alloys under high-strain shear deformation. *Materialia* **2021**, *18*, 101146.
(33) Pouryazdan, M.; Kaus, B. J. P.; Rack, A.; Ershov, A.; Hahn, H. Mixing instabilities during shearing of metals. *Nat. Commun.* **2017**, *8*, 1611.
(34) Hohenberg, P.; Kohn, W. Inhomogeneous Electron Gas. *Phys. Rev.* **1964**, *136*, B864−B871.
(35) Kohn, W.; Sham, L. J. Self-Consistent Equations Including Exchange and Correlation Effects. *Phys. Rev.* **1965**, *140*, A1133−A1138.
(36) Kresse, G.; Furthmüller, J. Efficient iterative schemes for ab initio total-energy calculations using a plane-wave basis set. *Phys. Rev. B: Condens. Matter Mater. Phys.* **1996**, *54*, 11169−11186.
(37) Kresse, G.; Furthmüller, J. Efficiency of ab-initio total energy calculations for metals and semiconductors using a plane-wave basis set. *Phys. Rev. B: Condens. Matter Mater. Phys.* **1996**, *54*, 11169−11186.
(38) Kresse, G.; Hafner, J. Ab initio molecular dynamics for liquid metals. *Phys. Rev. B: Condens. Matter Mater. Phys.* **1993**, *47*, 558−561.
(39) Kresse, G.; Hafner, J. Ab initio molecular-dynamics simulation of the liquid-metal-amorphous-semiconductor transition in germa-

https://doi.org/10.1021/acsomega.1c07368
ACS Omega 2022, 7, 13721−13736

nium. *Phys. Rev. B: Condens. Matter Mater. Phys.* **1994**, *49*, 14251−14269.
(40) Perdew, J. P.; Burke, K.; Ernzerhof, M. Generalized Gradient Approximation Made Simple. *Phys. Rev. Lett.* **1996**, *77*, 3865−3868.
(41) Perdew, J. P.; Burke, K.; Ernzerhof, M. Generalized Gradient Approximation Made Simple [Phys. Rev. Lett. 77, 3865 (1996)]. *Phys. Rev. Lett.* **1997**, *78*, 1396.
(42) Blöchl, P. E. Projector augmented-wave method. *Phys. Rev. B: Condens. Matter Mater. Phys.* **1994**, *50*, 17953−17979.
(43) Tang, W.; Sanville, E.; Henkelman, G. A grid-based Bader analysis algorithm without lattice bias. *J. Phys. Condens. Matter* **2009**, *21*, 075307.
(44) Sanville, E.; Kenny, S. D.; Smith, R.; Henkelman, G. Improved grid-based algorithm for Bader charge allocation. *J. Comput. Chem.* **2007**, *28*, 899−908.
(45) Henkelman, G.; Arnaldsson, A.; Jónsson, H. A fast and robust algorithm for Bader decomposition of charge density. *Comput. Mater. Sci.* **2006**, *36*, 354−360.
(46) Yu, M.; Trinkle, D. R. Accurate and efficient algorithm for Bader charge integration. *J. Chem. Phys.* **2011**, *134*, 064111.
(47) Swanson, H. E.; Tatge, E.. *Standard X-ray Diffraction Powder Patterns*; US Department of Commerce, National Bureau of Standards, 1953; Vol. *539*, p 1.
(48) Straumanis, M. E.; Zyszczynski, S. Lattice parameters, thermal expansion coefficients and densities of Nb, and of solid solutions Nb−O and Nb−N−O and their defect structure. *J. Appl. Crystallogr.* **1970**, *3*, 1−6.
(49) Archard, J. Elastic deformation and the laws of friction. *Proc. Roy. Soc. Lond. Math. Phys. Sci.* **1957**, *243*, 190−205.
(50) Kauzlarich, J. J.; Williams, J. A. Archard wear and component geometry. *Proc. Inst. Mech. Eng., Part J* **2001**, *215*, 387−403.
(51) Rupert, T. J.; Schuh, C. A. Sliding wear of nanocrystalline Ni−W: structural evolution and the apparent breakdown of Archard scaling. *Acta Mater.* **2010**, *58*, 4137−4148.
(52) Li, N.; Wang, J.; Misra, A.; Zhang, X.; Huang, J. Y.; Hirth, J. P. Twinning dislocation multiplication at a coherent twin boundary. *Acta Mater.* **2011**, *59*, 5989−5996.
(53) Yasunaga, K.; Iseki, M.; Kiritani, M. Dislocation structures introduced by high-speed deformation in bcc metals. *Mater. Sci. Eng. A* **2003**, *350*, 76−80.
(54) Wang, K.; Tao, N. R.; Liu, G.; Lu, J.; Lu, K. Plastic strain-induced grain refinement at the nanometer scale in copper. *Acta Mater.* **2006**, *54*, 5281−5291.
(55) Miura, H.; Nakao, Y.; Sakai, T. Enhanced grain refinement by mechanical twinning in a bulk Cu-30 mass% Zn during multi-directional forging. *Mater. Trans.* **2007**, *48* (9), 2539−2541.
(56) Lu, N.; Du, K.; Lu, L.; Ye, H. Q. Transition of dislocation nucleation induced by local stress concentration in nanotwinned copper. *Nat. Commun.* **2015**, *6*, 7648.
(57) Mayeur, J. R.; Beyerlein, I. J.; Bronkhorst, C. A.; Mourad, H. M.; Hansen, B. L. A crystal plasticity study of heterophase interface character stability of Cu/Nb bicrystals. *Int. J. Plast.* **2013**, *48*, 72−91.
(58) Mayeur, J. R.; Beyerlein, I. J.; Bronkhorst, C. A.; Mourad, H. M. Incorporating interface affected zones into crystal plasticity. *Int. J. Plast.* **2015**, *65*, 206−225.
(59) Jia, N.; Raabe, D.; Zhao, X. Crystal plasticity modeling of size effects in rolled multilayered Cu-Nb composites. *Acta Mater.* **2016**, *111*, 116−128.
(60) Chen, T.; Yuan, R.; Beyerlein, I. J.; Zhou, C. Predicting the size scaling in strength of nanolayered materials by a discrete slip crystal plasticity model. *Int. J. Plast.* **2020**, *124*, 247−260.
(61) Sahu, S.; Sharma, N. K.; Patel, S. K.; Mondal, K.; Shekhar, S. The effect of grain boundary structure on sensitization behavior in a nickel-based superalloy. *J. Mater. Sci.* **2019**, *54*, 1797−1818.
(62) Sahu, S.; Yadav, P. C.; Shekhar, S. Use of hot rolling for generating low deviation twins and a disconnected random boundary network in inconel 600 alloy. *Metall. Mater. Trans.* **2018**, *49*, 628−643.
(63) Dautzenberg, J. H.; Zaat, J. H. Quantitative determination of deformation by sliding wear. *Wear* **1973**, *23*, 9−19.
(64) Hughes, D. A.; Hansen, N. High angle boundaries formed by grain subdivision mechanisms. *Acta Mater.* **1997**, *45*, 3871−3886.
(65) Beach, J. A.; Wang, M.; Bellon, P.; Dillon, S.; Ivanisenko, Y.; Boll, T.; Averback, R. S. Self-organized, size-selection of precipitates during severe plastic deformation of dilute Cu-Nb alloys at low temperatures. *Acta Mater.* **2017**, *140*, 217−223.
(66) Vo, N. Q.; Schäfer, J.; Averback, R. S.; Albe, K.; Ashkenazy, Y.; Bellon, P. Reaching theoretical strengths in nanocrystalline Cu by grain boundary doping. *Scr. Mater.* **2011**, *65*, 660−663.
(67) Raabe, D.; Mattissen, D. Microstructure and mechanical properties of a cast and wire-drawn ternary Cu−Ag−Nb in situ composite. *Acta Mater.* **1998**, *46*, 5973−5984.
(68) Ohsaki, S.; Raabe, D.; Hono, K. Mechanical alloying and amorphization in Cu−Nb−Ag in situ composite wires studied by TEM and atom probe tomography. *MRS 2009 Fall Meeting*; MRS, 2009.

https://doi.org/10.1021/acsomega.1c07368
ACS Omega 2022, 7, 13721−13736